scientific reports

Check for updates

OPEN

Metastability relationship between two- and three-dimensional crystal structures: a case study of the Cu-based compounds

Shota Ono

Some of the three-dimensional (3D) crystal structures are constructed by stacking two-dimensional (2D) layers. To study whether this geometric concept, i.e., using 2D layers as building blocks for 3D structures, can be applied to computational materials design, we theoretically investigate the dynamical stability of copper-based compounds Cu*X* (a metallic element *X*) in the B_h and $L1_1$ structures constructed from the buckled honeycomb (BHC) structure and in the B2 and $L1_0$ structures constructed from the buckled square (BSQ) structure. We demonstrate that (i) if Cu*X* in the BHC structure is dynamically stable, those in the B_h and $L1_1$ structures are also stable. Using molecular dynamics simulations, we particularly show that CuAu in the B_h and $L1_1$ structures withstand temperatures as high as 1000 K. Although the interrelationship of the metastability between the BSQ and the 3D structures (B2 and $L1_0$) is not clear, we find that (ii) if Cu*X* in the B2 ($L1_0$) structure is dynamically stable, that in the $L1_0$ (B2) is unstable. This is rationalized by the tetragonal Bain path calculations.

Since the synthesis of many atomically thin materials, the two-dimensional (2D) structure has been regarded as one of the metastable structures in materials science, as a result of which the database including several 2D structures can now be available[1–5]. Many 2D materials can be exfoliated from their three-dimensional (3D) counterparts, as the relation between the graphene and the graphite, in turn, implying that the 2D layers can be building blocks for constructing the 3D crystal structures. Recently, 2D CuAu has been synthesized experimentally[6], where it consists of the hexagonal Cu and Au monolayers, forming the buckled honeycomb (BHC) structure. By considering the 2D CuAu as a building block for the 3D structures, one can construct the B_h and $L1_1$ structures with the ABAB and ABC stacking methods, respectively (see Fig. 1). However, the synthesis of CuAu in these structures have not yet been reported.

The stability of the 2D metals has recently been studied in detail[7–15]. By focusing on the 2D elemental metals, the author has demonstrated that the concept above (i.e., the 2D structure as a building block for the 3D structures) can hold by using first principles calculations: If the planar hexagonal (HX) structure is dynamically stable, then the BHC, the fcc, and/or the hcp structures are also stable[13]. Po in the square lattice structure is dynamically stable[14], as a counterpart of Po in the simple cubic structure. More recently, the author has also demonstrated that if a compound in the B_h structure has been synthesized experimentally, that in the BHC structure is dynamically stable[15]. These studies motivate us to study the metastability relationship between the 2D and 3D compounds in detail.

Of particular interest is the Cu-based compounds because since the discovery of $L1_0$-type CuAu, many crystal structures of those compounds have been studied for many years. For the binary compounds of Cu*X*, where *X* is an element in the periodic table, several phases have been synthesized experimentally: CuBe[16], CuPd[17], CuSc[18], CuY[19], CuZn[20], and CuZr[21] in the B2 (CsCl-type) structure, CuCl, CuBr, and CuI[22] in the B3 (zincblend-type) structure, CuAu[23] in the $L1_0$ structure, and CuPt[24] in the $L1_1$ structure. These structures are interrelated with each other by the following deformations: The tetragonal Bain distortion elongating the *c* axis transforms the B2 into the $L1_0$ structure (see Fig. 1); the trigonal distortion elongating the (111) axis transforms the B2 structure into, via the B1 (NaCl-type) structure, the $L1_1$ structure (see Fig. 1); and by shortening the interatomic distance along

Department of Electrical, Electronic and Computer Engineering, Gifu University, Gifu 501-1193, Japan. email: shota_o@gifu-u.ac.jp

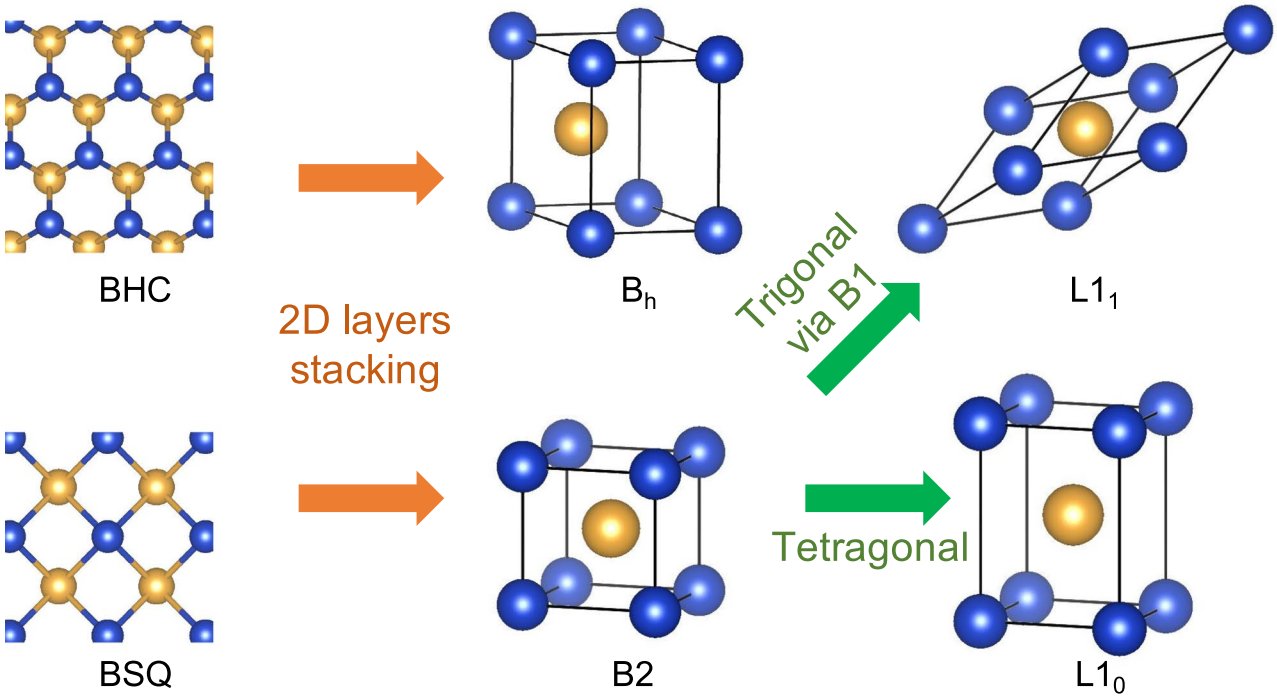

Figure 1. Illustrations of the 2D (BHC and BSQ) and 3D structures (B_h, $L1_1$, B2, and $L1_0$) and its interrelationships: Stacking the 2D structures vertically produces the 3D structures and the tetragonal and trigonal distortions of the B2 structure yield the $L1_0$ and $L1_1$ structures, respectively.

the (111) axis the B1 is transformed into the B3 structure. In this way, the existence of Cu*X* in the B_h structure has not yet been explored. Note also that among binary metallic phases, $L1_1$ as well as B_h structures are quite rare structure, as has been pointed out in Ref.[25] and observed in AlSn solid solutions[26]. Therefore, it will be interesting to study whether the design of Cu*X* is possible based on the geometric concept (i.e., from 2D to 3D) combined with the dynamical stability analysis beyond the formation energy analysis[25].

In this paper, we investigate the interrelationship of the dynamical stability between the 2D and the 3D structures by focusing on Cu*X* with a metallic element *X*. By calculating the phonon density-of-states (DOS) from first principles, we demonstrate that if Cu*X* in the BHC structure is dynamically stable, Cu*X* in the B_h and $L1_1$ structures are also stable. This indicates that the BHC structure serves as a building block for the B_h and $L1_1$ structures, while in some compounds the dynamical stability of the B_h and $L1_1$ structures relies on the coupling between the BHC structures along the *c* axis. By performing the molecular dynamics simulations, we particularly show that CuAu in the B_h and $L1_1$ structures are stable up to 1000 K.

We also study the dynamical stability of Cu*X* in the the buckled square (BSQ), B2, and $L1_0$ structures, where the latter two structures can be constructed by stacking the BSQ structures (see Fig. 1). However, we find it difficult to discuss the metastability relationship between the 2D and 3D tetragonal structures because most of Cu*X* in the BSQ structure are unstable. Analogous to the instability of the bcc (fcc) elemental metals in the fcc (bcc) structure[27], we can find that if Cu*X* in the B2 ($L1_0$) structure is dynamically stable, that in the $L1_0$ (B2) structure is unstable. This is visualized by means of the tetragonal Bain path calculations.

The metastability relationships between different crystal structures are summarized in Table 1: The first two relationships between the fcc, hcp and bcc structures can be applicable to the stability of elemental metals[27]; the third is the relationship between the 2D elemental metals; the fourth and fifth are the relationships between the 2D and 3D elemental metals; and the others are the relationships between the 2D and 3D compounds. It has been shown that the (m, n) Lennard-Jones crystals also satisfy the first and the fifth relationships when $m + n \geq 18$, i.e., the short-ranged potentials[28]. We hope that the present study paves the way to computational materials design based on the interrelationship between the 2D and 3D structures. Making the metastability database for other compounds *XY* and exploring other 2D structures as building blocks for the 3D structures are left for future work.

The present study will serve as one of the geometry-based approaches that have been proposed in computational materials science. Hart et al. have generated superstructures as a derivative of a parent crystal structure[29]. In contrast, Kolli et al. have mapped complex crystal structures onto several parent structures[30]. They have pointed out that 15 of the top 20 parent structures can be generated by vertically stacking simple 2D structures including the close-packed, honeycomb, kagome, square, and more complex structures. As an extension of the present investigation, these will be candidate structures for creating the metastability database of the ordered compounds *XY*.

Property 1	→	Property 2	Example
fcc and hcp stable	→	bcc unstable	group 3, 4, 10, and 11[27]
bcc stable	→	fcc and hcp unstable	group 5 and 6[27]
HX stable	→	BHC stable	group 2, 11, and 12[13]
HX stable	→	fcc and hcp stable	group 2, 11, and 12[13]
BSQ stable	→	fcc and hcp stable	group 3, 7, 8, 9, and 10 and Al[13]
B_h synthesized	→	BHC stable	IrLi, LiPd, LiPt, and LiRh[15]
BHC stable	→	B_h and $L1_1$ stable	CuX with X = Li, W, Co, Ni, Cu, Ag, Au, Zn, and Al (this work)
B2 stable	→	$L1_0$ unstable	CuX with X = K, Rb, group 2 and 3, and Pd (this work)
$L1_0$ stable	→	B2 unstable	CuX with X = Li, group 5 and 6, Mn, Tc, Fe, Ru, group 9, Ni, Pt, Cu, Au,
			Zn, and Ga (this work)

Table 1. The interrelationship of the dynamical stability between different structures. The "stable" structure has no imaginary frequencies within the phonon Brillouin zone.

	1	2	3	4	5	6	7	8	9	10	11	12	13	14
2	Li BHC B_h $L1_1$	Be - B_h $L1_1$	CuX BHC B_h $L1_1$										B	C
3	Na - - -	Mg - - -											Al BHC B_h $L1_1$	Si
4	K - - -	Ca - - -	Sc - - -	Ti - - -	V - B_h $L1_1$	Cr - $L1_1$	Mn - B_h -	Fe - B_h $L1_1$	Co BHC B_h $L1_1$	Ni BHC B_h $L1_1$	Cu BHC B_h $L1_1$	Zn BHC B_h $L1_1$	Ga - B_h $L1_1$	Ge
5	Rb - - -	Sr - - $L1_1$	Y - - -	Zr - - -	Nb - - $L1_1$	Mo - - $L1_1$	Tc - B_h -	Ru - B_h $L1_1$	Rh - B_h $L1_1$	Pd - B_h $L1_1$	Ag BHC B_h $L1_1$	Cd - - -	In - - -	Sn - - -
6	Cs - - -	Ba - - $L1_1$	Lu - - -	Hf - - -	Ta - - $L1_1$	W BHC B_h $L1_1$	Re - B_h $L1_1$	Os - B_h $L1_1$	Ir - B_h $L1_1$	Pt - B_h $L1_1$	Au BHC B_h $L1_1$	Hg - - -	Tl - - -	Pb - - -

Figure 2. Periodic table for the CuX compounds in the BHC, B_h, and $L1_1$ structures. The dynamically stable structure *j*s are indicated. CuX with X = Ca, Sr, Ba, Sc, Y, and Lu has the B1 structure rather than the $L1_1$ structure as a dynamically stable or unstable structure (see the Supplementary Information).

Results and discussion

BHC, B_h, and $L1_1$. The resultant dynamical stability properties are summarized in the periodic table of Fig. 2. The phonon DOS of CuX in the BHC, B_h, and $L1_1$ structures are provided in the Supplementary Information. For the case of X = Cu, the B_h and $L1_1$ structures correspond to the hcp and fcc structures, respectively. The main finding is that if the BHC structure is dynamically stable, then the B_h and $L1_1$ structures are also stable, as in the cases of X = Li, W, Co, Ni, Cu, Ag, Au, Zn, and Al (dark green). On the other hand, if the B_h and $L1_1$ structures are unstable, the BHC structure is also unstable (gray). These indicate that the BHC structure serves as a building block for the B_h as well as $L1_1$ structures. For some compounds (light green, light red, and yellow), only the B_h and/or $L1_1$ structures are dynamically stable. This implies that the layer stacking vertically suppresses the instability against the out-of-plane vibrations in thin films, while the prediction of such a critical thickness is beyond the scope of the present work.

BSQ, B2, and $L1_0$. We next study the dynamical stability of CuX in the BSQ, B2, and $L1_0$ structures. The phonon DOS of these structures are also provided in the Supplementary Information. As shown in Fig. 3, only CuBe, CuRh, and CuCu in the BSQ structure are dynamically stable, while most of CuX in the B2 or $L1_0$ structures are dynamically stable. Therefore, it seems to be difficult to find a useful relationship of the dynamical stability between the BSQ and the 3D structures. Interestingly, one can find that if CuX in the B2 structure is dynamically stable, that in the $L1_0$ structure is unstable, and vice versa: if CuX in the $L1_0$ structure is dynamically stable, that in the B2 structure is unstable. This is analogous to the metastability relationship between the bcc and the fcc structures in the elemental metals listed in Table 1. This will be rationalized by the tetragonal Bain path calculations below.

	1	2	3	4	5	6	7	8	9	10	11	12	13	14
2	Li - - $L1_0$	Be BSQ B2 -	CuX BSQ B2 $L1_0$										B	C
3	Na - - -	Mg - B2 -											Al - - -	Si
4	K - B2 -	Ca - B2 -	Sc - B2 -	Ti - - -	V - - $L1_0$	Cr - - $L1_0$	Mn - - $L1_0$	Fe - - $L1_0$	Co - - $L1_0$	Ni - - $L1_0$	Cu BSQ - $L1_0$	Zn - - $L1_0$	Ga - - $L1_0$	Ge
5	Rb - B2 -	Sr - B2 -	Y - B2 -	Zr - - -	Nb - - $L1_0$	Mo - - $L1_0$	Tc - - $L1_0$	Ru - - $L1_0$	Rh BSQ - $L1_0$	Pd - B2 -	Ag - - -	Cd - - -	In - - -	Sn - - -
6	Cs - - -	Ba - B2 -	Lu - B2 -	Hf - - -	Ta - - $L1_0$	W - - $L1_0$	Re - - -	Os - - -	Ir - - $L1_0$	Pt - - $L1_0$	Au - - $L1_0$	Hg - - -	Tl - - -	Pb - - -

Figure 3. Same as in Fig. 2 but for the CuX compounds in the BSQ, B2, and $L1_0$ structures.

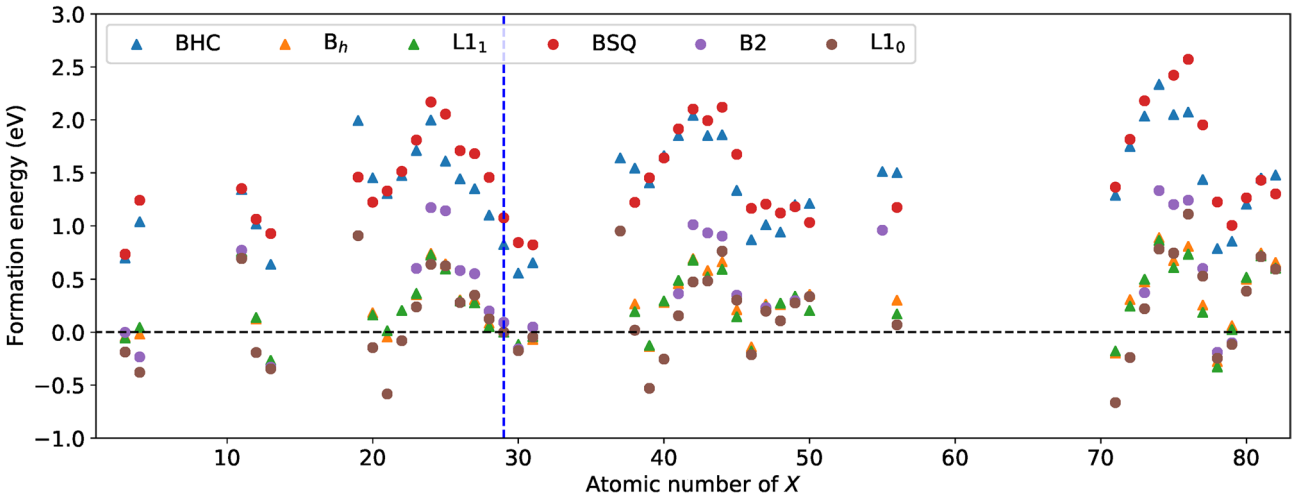

Figure 4. The formation energy (per a unit cell including two atoms) of CuX in the BHC, B_h, $L1_1$, BSQ, B2, and $L1_0$. The vertical dashed line (blue) indicates the case of X = Cu.

In the present study, CuX in the B2 structure for X = group 1 (K and Rb), group 2 (Be, Mg, Ca, Sr, and Ba), group 3 (Sc, Y, and Lu), and Pd have been identified to be dynamically stable. In contrast, CuBe[16], CuSc[18], CuY[19], CuZr[21], CuPd[17], and CuZn[20] in the B2 structure have been synthesized experimentally at ambient condition. For the case of the $L1_0$ structure, 20 CuX in the $L1_0$ structure have been predicted to be dynamically stable, whereas only CuAu has been synthesized experimentally[23]. It has been shown that the lowest energy phonon at the R point, $(0, \pi/a, \pi/c)$, of the $L1_0$ CuAu is stabilized by the long-range interatomic interactions from the first to more than the fifth nearest neighbors[31]. If the same scenario holds, the stabilization of the phonons at the N point, $(0, \pi/a, \pi/a)$, and the R point will be a key to synthesize the ordered compounds in the B2 and $L1_0$ structures, respectively.

Formation energy. As a measure of relative stability compared to elemental metals Cu and X, Fig. 4 plots the formation energies E_j(CuX) defined as Eq. (1) for j = BHC, B_h, and $L1_1$ (triangles) and for j = BSQ, B2, and $L1_0$ (circles). The CuX in the BHC and BSQ structures have positive E_j and those in the 3D structures are energetically more stable. The B_h and/or $L1_1$ structures have negative E_j for X = Li, Be, Sc, Y, Lu, Pd, Pt, Zn, Al, and Ga, while the B2 and/or $L1_0$ structures have negative E_j for X = Li, Be, Mg, Ca, Sc, Y, Lu, Ti, Zr, Pd, Pt, Au, Zn, Al, and Ga. The group-dependence of the energetic stability is observed, that is, the CuXs with the group 2, 3, 12, and 13 elements of X tend to have low energy, while those with the group 6 elements of X have high energy. This tendency is similar to that predicted for the Pb- and Sn-based compounds[32].

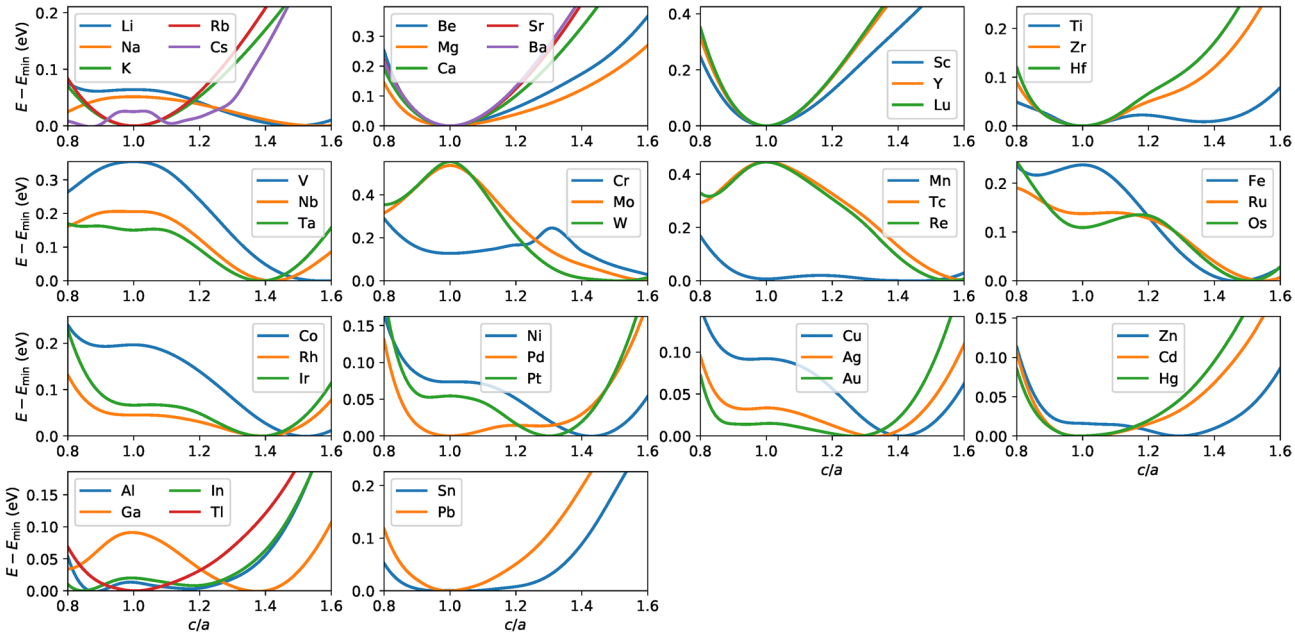

Figure 5. The total energy per a cell as a function of c/a (the tetragonal path) for CuX.

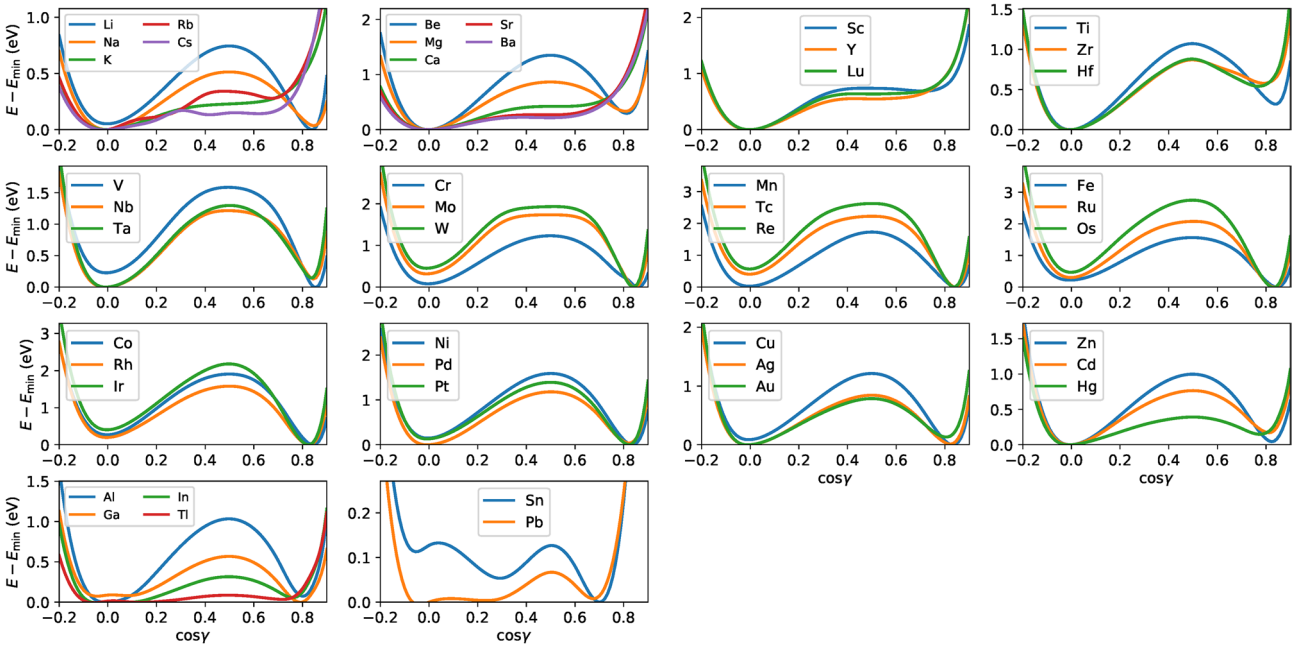

Figure 6. The total energy per a cell as a function of cosγ (the trigonal path) for CuX.

Tetragonal and trigonal paths. To understand the metastability relationship between the B2 and the $L1_0$ structures proposed above, we show the total energy curves along the tetragonal Bain path in Fig. 5, where the volume of CuX is fixed to that of the B2 structure. If the total energy takes the minimum value at $c/a = 1$ (B2), no energy minimum is observed at $c/a > 1$ ($L1_0$), as for $X =$ K, Rb, group 2, and group 3. In contrast, if the total energy takes the minimum value at $c/a > 1$, then that takes the maximum or higher values at $c/a = 1$. It should be noted that the anomalous stability of CuPd in the B2 structure (see the group 10 in Fig. 3) can be understood as the shift of the energy minimum to $c/a = 1$.

The B2 structure can be transformed into the $L1_1$ structure through the trigonal path, elongating or shortening the cubic structure along the (111) direction with the volume fixed to that of the B2 structure. Figure 6 shows the total energy as a function of cos γ, where γ is the angle between the primitive lattice vectors (see Methods for the details). For most of X, one can observe a double well-like energy curve with a potential energy barrier height of about 1 eV, indicating that the B2 ($\cos\gamma = 0$) and $L1_1$ ($\cos\gamma \simeq 0.8$) structures are energetically stable. The energy maximum at $\cos\gamma = 0.5$ corresponds to the B1 structure. For $X =$ Ca, Sr, Ba, Sc, Y, and Lu, the

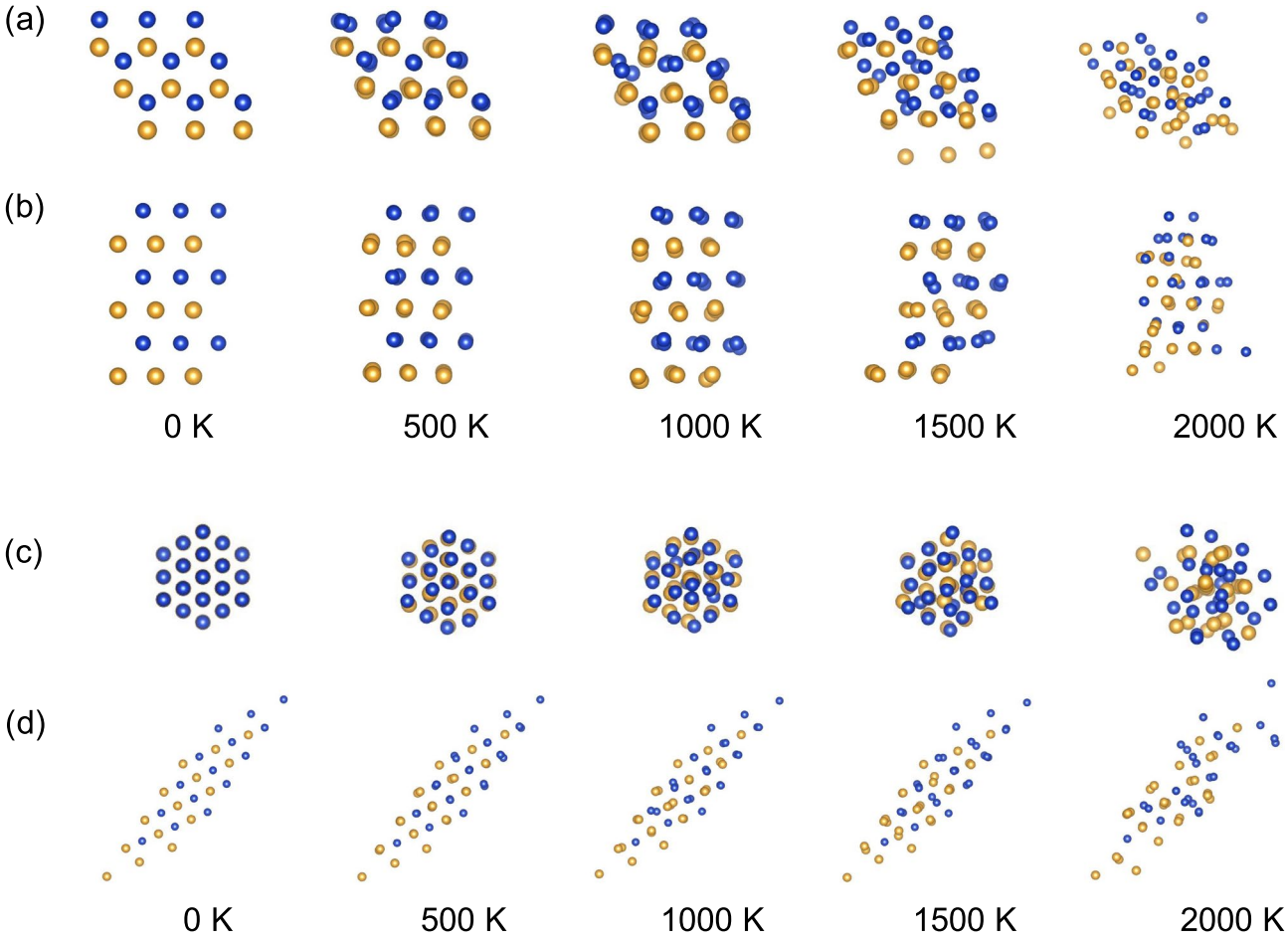

Figure 7. The atomic distribution of the CuAu compounds after the MD simulation of 5 ps (B_h) and 4 ps ($L1_1$) for several Ts: (**a**) Top and (**b**) side views of the B_h structure and (**c**) top and (**d**) side views of the $L1_1$ structure.

energy curve around $\cos\gamma = 0.5$ is almost flat. In these compounds, the $L1_1$ structure was transformed into the B1 structure after the geometry optimization (see the Supplementary Information).

The stability properties of CuX along the tetragonal and trigonal paths in Figs. 5 and 6 are almost consistent with those in Figs. 2 and 3. However, the energetic stability along the tetragonal and trigonal paths may not guarantee the dynamical stability of the structure[27,33]. This is because the phonon calculations investigate whether the Hessian of the potential energy is positive definite around the crystal structure considered, whereas the transformation path calculations restrict atomic displacements to only one distortion direction assumed. For X = Ti, Zr, and Hf (group 4), although the trigonal path calculations predict that the B2 and $L1_1$ structures are stable, CuX in those structures are unstable (see Figs. 2 and 3). This implies that other transformation paths may exist, i.e., the compound will show a phase transformation due to a negative curvature in the potential energy surface around the B2 and $L1_1$ structures. It will be desirable to perform more systematic calculations that investigate the interrelationship between metastable structures, as demonstrated in elemental metals[34].

CuAu in the B_h and $L1_1$ structures. The experimental synthesis of the BHC CuAu has been reported recently[6]. Based on the phonon calculations, we confirmed that such a structure is dynamically stable[15] and predicted that the B_h and $L1_1$ structures are also dynamically stable, as they are constructed from the 2D structures. We discuss the temperature effect on the stability in the 3D structures below.

For the B_h structure, the lattice parameters are $a = 2.858$ Å and $c/a = 1.526$. For the $L1_1$ structure, the lattice parameter is $a = 4.726$ Å and the primitive vectors are (u, v, v), (v, u, v), and (v, v, u) in units of $a/\sqrt{3}$ with $u = 0.239$ and $v = 0.669$. The total energy of the B_h and $L1_1$ structures are energetically higher than that of the $L1_0$ structure, the ground state structure of CuAu, by 0.176 eV and 0.138 eV per a cell. These values are much higher than the thermal energy at the ambient condition. As shown in Fig. 6, the potential barrier height ($\sim$ 1 eV) between the $L1_1$ and the B2 ($\simeq L1_0$) structures is also high enough not to yield the phase transition. Therefore, once synthesized, these metastable structures will be stable.

Figure 7(a) and (b) shows the temperature (T)-dependence of the atomic distribution in the B_h supercell at the end of the molecular dynamics (MD) simulation (5 ps). The B_h structure is stable up to $T = 1000$ K because the structure of each layer (i.e., the 2D hexagonal layer of Au and Cu) is still preserved. When $T = 1500$ K, the hexagonal symmetry in each layer is broken. When T is increased to 2000 K, the atomic displacements are

X	BHC	B_h	$L1_1$	BSQ	B2	$L1_0$
Cr	0.00	0.00	0.00	0.00	3.47	0.00
Mn	3.83	2.98	0.00	0.00	0.00	0.00
Fe	2.64	2.55	2.54	2.80	2.66	2.71
Co	1.70	1.67	1.65	1.84	1.53	1.74
Ni	0.47	0.30	0.00	0.55	0.41	0.43

Table 2. The total magnetic moment of CuX (X = Cr, Mn, Fe, Co, and Ni) in the structure j. The figures are in units of μ_B per a cell (μ_B the Bohr magneton).

significant, so that the layered structure is not observed. Similar tendency is observed in the $L1_1$ structure after the MD simulation of 4 ps, as shown in Fig. 7(c) and (d).

Methods

The total energy and the optimized structures of CuX were calculated within the density-functional theory implemented in Quantum ESPRESSO (QE)[35]. We used the exchange-correlation functional of Perdew, Burke, and Ernzerhof (PBE)[36] and the ultrasoft pseudopotentials in pslibrary.1.0.0[37]. We used the cutoff energies of 80 and 800 Ry for the wavefunction and the charge density, respectively, used $20 \times 20 \times 1$ k grid and $20 \times 20 \times 20$ k grid for 2D and 3D structures, respectively[38], and set the smearing parameter of $\sigma = 0.02$ Ry[39]. For the BHC and BSQ structures, the size of the unit cell along the c axis was set to be 14 Å to avoid the spurious interaction between different unit cells. For the geometry optimization of the BHC, B_h, BSQ, B2, and $L1_0$ structures, the initial guess of the lattice parameters was set to the same as the optimized value obtained by our previous calculations[15]. The optimization calculations of the $L1_1$ structure was started by assuming $\cos\gamma = 0.82$ ($\gamma = 35°$ between the primitive lattice vectors) and the unit cell volume equal to that of the B_h structure.

For the tetragonal Bain path calculations, we first calculated the unit cell volume of the B2 structure, $\Omega_0 = a_0^3$ with the optimized lattice parameter a_0, and next deformed the shape of the unit cell but by keeping the volume $\Omega_0 = a^2 c$ fixed, where the primitive lattice vectors are defined as $(a, 0, 0)$, $(0, a, 0)$, and $(0, 0, c)$. For the trigonal Bain path calculations, we also fixed the unit cell volume to be Ω_0. By setting the input parameter `ibrav` to -5 in QE[35], we defined the primitive lattice vectors as (u, v, v), (v, u, v), and (v, v, u) in units of $a/\sqrt{3}$. Given a parameter $c = \cos\gamma = (v^2 + 2uv)/(u^2 + 2v^2)$ that is equal to the cosine of the angle between any pairs of primitive lattice vectors, in turn, we determined the values of a, u, and v by using the relations $\Omega_0 = a^3(1-c)\sqrt{1+2c}$, $u = \sqrt{(1+2c)/3} - 2\sqrt{(1-c)/3}$, and $v = \sqrt{(1+2c)/3} + \sqrt{(1-c)/3}$.

We performed the spin-polarized calculations, where the total energy and forces are converged within 10^{-5} Ry and 10^{-4} a.u., respectively, which are smaller than the default values by a factor of ten. In our previous study, we performed the spin-unpolarized calculations by using the default values of the convergence criteria[15]. In the spin-polarized calculations, the finite magnetic moment was observed for CuX with X = Cr, Mn, Fe, Co, and Ni when a ferromagnetic state was assumed as an initial guess. As listed in Table 2, the size of the magnetic moment in the BHC and BSQ structures seems to be larger than that in their 3D counterparts. We also found that a few compounds show a finite magnetic moment: For the BHC structure, CuTi (0.87); for the B2 structure, CuHg (0.47), CuIr (0.47), CuRe (2.28), CuRh (1.02), and CuZr (0.01); and for the $L1_0$ structure, CuHf (0.01), CuRh (0.72), and CuZr (0.05), where the figure in parenthesis is in units of μ_B per a cell. It has been shown that the 2D elemental metals of Ba, group 2 (Sc and Y), group 3 (Ti, Zr, and Hf), V, group 8 (Ru and Os), group 9 (Rh and Ir), and group 10 (Pd and Pt) can have a finite magnetic moment[12]. This has been attributed to a decrease in the coordination number as well as a change in the electron DOS shape. Therefore, it will be helpful to study the effect of the electronic band structure on the dynamical stability of CuX, in addition to the geometric concept investigated in the present work. It will also be interesting to study the competition of the energetic stability between the ferromagnetic and antiferromagnetic phases in a systematic manner. However, these are beyond the scope of the present work.

The formation energy of CuX in the structure j per a unit cell including two atoms was calculated by

$$E_j(\mathrm{Cu}X) = \varepsilon_j(\mathrm{Cu}X) - \frac{1}{2}[\varepsilon_{\min}(\mathrm{Cu}) + \varepsilon_{\min}(X)], \tag{1}$$

where $\varepsilon_j(\mathrm{Cu}X)$ is the total energy of CuX in the structure j. $\varepsilon_{\min}(X)$ is the minimum total energy of X, where this is determined by calculating the energy of the bcc, fcc, and hcp structures. Note that the functional dependence of the E_j of ordered compounds has been studied in detail[41–44]. The use of the PBE functional can predict the value of E_j accurately for strongly bonded systems, while it may underestimate E_j for weakly bonded systems such as CuAu. The calculated values of E_j as well as those in the Materials Project (MP) database[40] were provided in the Supplementary Information.

To show the numerical accuracy within the PBE calculations, we compared the lattice parameters with those in the MP database[40], and the experimental values for the B2, $L1_0$, and $L1_1$ structures, as listed in Table 3. Except for CuPt, the agreement between the present calculations, the MP database[40], and the experiment is good (the deviation is less ± 0.03 Å). The lattice parameters of CuX in the structure j were also provided in the Supplementary Information.

X	This work	MP[40]	Experiment
Be	2.69	2.69	2.70[16]
Pd	3.01	3.02	2.98[17]
Sc	3.26	3.26	3.26[18]
Y	3.48	3.48	3.48[19]
Zn	2.96	2.96	2.95[20]
Zr	3.27	3.27	3.26[21]
Au (*a*)	2.87	2.86	2.85[23]
Au (*c*)	3.64	3.66	3.67[23]
Pt (*a*)	2.87	2.75	3.13[24]
Pt (*c*)	12.91	12.86	14.98[24]

Table 3. The lattice parameters of Cu*X* in the B2 structure, CuAu in the $L1_0$ structure, and CuPt in the $L1_1$ structure. For the $L1_1$ structure, the parameters of the conventional unit cell (including six atoms) are listed.

The dynamical stability and the instability of Cu*X* in the structure *j* were determined by the phonon DOS calculations within the density-functional perturbation theory[45] implemented in the QE code[35]. We used more than a $6 \times 6 \times 1$ *q* grid for the 2D structures (seven *q* points for the BHC and ten *q* points for the BSQ structures), $3 \times 3 \times 3$ *q* grid (six *q* points) for the B_h and $L1_0$ structures, $3 \times 3 \times 3$ *q* grid (four *q* points) for the B2 structure, and $2 \times 2 \times 2$ *q* grid (four *q* points) for the $L1_1$ structure.

For the case of CuAu in the B_h and $L1_1$ structures, the MD simulation was performed by using the QE[35]. The $3 \times 3 \times 3$ supercell (54 atoms) was used by considering only the Γ point in the Brillouin zone. The ionic temperature *T* is controlled by the velocity scaling method, where $T = 500$, 1000, 1500, and 2000 K were assumed. The time step of the MD simulation was set to 20 a.u. (0.96 fs) and the number of the steps was set to 5250 (5.08 ps) and 4200 (4.06 ps) for the B_h and $L1_1$ structures, respectively.

Received: 21 May 2021; Accepted: 6 July 2021
Published online: 16 July 2021

References

1. Ashton, M., Paul, J., Sinnott, S. B. & Hennig, R. G. Topology-scaling identification of layered solids and stable exfoliated 2D materials. *Phys. Rev. Lett.* **118**, 106101. https://doi.org/10.1103/PhysRevLett.118.106101 (2017).
2. Choudhary, K., Kalish, I., Beams, R. & Tavazza, F. High-throughput identification and characterization of two-dimensional materials using density functional theory. *Sci. Rep.* **7**, 5179. https://doi.org/10.1038/s41598-017-05402-0 (2017).
3. Haastrup, S. *et al.* The computational 2D materials database: High-throughput modeling and discovery of atomically thin crystals. *2D Materials* **5**, 042002. https://doi.org/10.1088/2053-1583/aacfc1 (2018).
4. Zhou, J. *et al.* 2DMatPedia, an open computational database of two-dimensional materials from top-down and bottom-up approaches. *Sci. Data* **6**, 86. https://doi.org/10.1038/s41597-019-0097-3 (2019).
5. Fukuda, M., Zhang, J., Lee, Y.-T. & Ozaki, T. A structure map for AB_2 type 2D materials using high-throughput DFT calculations. *Mater. Adv.*https://doi.org/10.1039/D0MA00999G *(2021).*
6. Zagler, G. *et al.* CuAu, a hexagonal two-dimensional metal. *2D Materials* **7**, 045017. https://doi.org/10.1088/2053-1583/ab9c39 (2020).
7. Aktürk, E., Aktürk, O. U. & Ciraci, S. Single and bilayer bismuthene: Stability at high temperature and mechanical and electronic properties. *Phys. Rev. B* **94**, 014115. https://doi.org/10.1103/PhysRevB.94.014115 (2016).
8. Kochat, V. *et al.* Atomically thin gallium layers from solid-melt exfoliation. *Sci.Adv.* **4**, 1701373. https://doi.org/10.1126/sciadv.1701373 (2018).
9. Nevalaita, J. & Koskinen, P. Atlas for the properties of elemental two-dimensional metals. *Phys. Rev. B* **97**, 035411. https://doi.org/10.1103/PhysRevB.97.035411 (2018).
10. Hwang, J., Oh, Y. J., Kim, J., Sung, M. M. & Cho, K. Atomically thin transition metal layers: Atomic layer stabilization and metal-semiconductor transition. *J. Appl. Phys.* **123**, 154301. https://doi.org/10.1063/1.5024200 (2018).
11. Wang, T., Park, M., Yu, Q., Zhang, J. & Yang, Y. Stability and synthesis of 2D metals and alloys: A review. *Mater. Today Adv.* **8**, 100092. https://doi.org/10.1016/j.mtadv.2020.100092 (2020).
12. Ren, Y. *et al.* Magnetism of elemental two-dimensional metals. *J. Mater. Chem. C* **9**, 4554–4561. https://doi.org/10.1039/D1TC00438G (2021).
13. Ono, S. Dynamical stability of two-dimensional metals in the periodic table. *Phys. Rev. B* **102**, 165424. https://doi.org/10.1103/PhysRevB.102.165424 (2020).
14. Ono, S. Two-dimensional square lattice polonium stabilized by the spin-orbit coupling. *Sci. Rep.* **10**, 11810. https://doi.org/10.1038/s41598-020-68877-4 (2020).
15. Ono, S. & Satomi, H. High-throughput computational search for two-dimensional binary compounds: Energetic stability versus synthesizability of three-dimensional counterparts. *Phys. Rev. B* **103**, L121403. https://doi.org/10.1103/PhysRevB.103.L121403 (2021).
16. Patskhverova, L. S. Nature of the δ phase in the copper-beryllium system. *Sov. Phys. J.* **12**, 646. https://doi.org/10.1007/BF00814859 (1969).
17. Subramanian, P. R. & Laughlin, D. E. Cu-Pd (Copper-Palladium). *J. Phase Equilib.* **12**, 231 (1991).
18. Aldred, A. T. Intermediate phases involving scandium. *Trans. Met. Soc. AIME* **224**, (1962).
19. Moriarty, J. L., Humphreys, J. E., Gordon, R. O. & Baenziger, N. C. X-ray examination of some rare-earth-containing binary alloy systems. *Acta Crystallogr.* **21**, 840. https://doi.org/10.1107/S0365110X6600402X (1966).
20. Shimizu, S., Murakami, Y. & Kachi, S. Lattice softening and martensitic transformation in Cu-Ni-Zn β phase alloys. *J. Phys. Soc. Jpn.* **41**, 79–84. https://doi.org/10.1143/JPSJ.41.79 (1976).

21. Carvalho, E. & Harris, I. Constitutional and structural studies of the intermetallic phase, ZrCu. *J. Mater. Sci.* **15**, 1224. https://doi.org/10.1007/BF00551811 (1980).
22. Hull, S. & Keen, D. A. High-pressure polymorphism of the copper(i) halides: A neutron-diffraction study to ~10 gpa. *Phys. Rev. B* **50**, 5868–5885. https://doi.org/10.1103/PhysRevB.50.5868 (1994).
23. Okamoto, H., Chakrabarti, D., Laughlin, D. & Massalski, T. B. The Au-Cu (Gold-Copper) system. *J. Phase Equilib.* **8**, 454. https://doi.org/10.1007/BF02893155 (1987).
24. Massalski, T. B., Okamoto, H., Subramanian, P. R. & Kacprzak, L. *Binary Alloy Phase Diagrams* 2nd edn. (American Society for Metals, Metals Park, OH, 1986).
25. Nelson, L. J., Hart, G. L. W. & Curtarolo, S. Ground-state characterizations of systems predicted to exhibit $L1_1$ or $L1_3$ crystal structures. *Phys. Rev. B* **85**, 054203. https://doi.org/10.1103/PhysRevB.85.054203 (2012).
26. Kane, R., Giessen, B. & Grant, N. New metastable phases in binary tin alloy systems. *Acta Metall.* **14**, 605–609. https://doi.org/10.1016/0001-6160(66)90068-X (1966).
27. Grimvall, G., Magyari-Köpe, B., Ozoliņš, V. & Persson, K. A. Lattice instabilities in metallic elements. *Rev. Mod. Phys.* **84**, 945–986. https://doi.org/10.1103/RevModPhys.84.945 (2012).
28. Ono, S. & Ito, T. Theory of dynamical stability for two- and three-dimensional Lennard-Jones crystals. *Phys. Rev. B* **103**, 075406. https://doi.org/10.1103/PhysRevB.103.075406 (2021).
29. Hart, G. L. W. & Forcade, R. W. Generating derivative structures from multilattices: Algorithm and application to hcp alloys. *Phys. Rev. B* **80**, 014120. https://doi.org/10.1103/PhysRevB.80.014120 (2009).
30. Kolli, S. K., Natarajan, A. R., Thomas, J. C., Pollock, T. M. & Van der Ven, A. Discovering hierarchies among intermetallic crystal structures. *Phys. Rev. Mater.* **4**, 113604. https://doi.org/10.1103/PhysRevMaterials.4.113604 (2020).
31. Ono, S. & Kobayashi, D. Lattice stability of ordered Au-Cu alloys in the warm dense matter regime. *Phys. Rev. B* **103**, 094114. https://doi.org/10.1103/PhysRevB.103.094114 (2021).
32. Ono, S., Yuhara, J. & Onoe, J. Theoretical prediction on the immiscible Pb-Sn alloy stabilized on metal surfaces. *Chem. Phys. Lett.* **776**, 138696. https://doi.org/10.1016/j.cplett.2021.138696 (2021).
33. Giret, Y., Daraszewicz, S. L., Duffy, D. M., Shluger, A. L. & Tanimura, K. Nonthermal solid-to-solid phase transitions in tungsten. *Phys. Rev. B* **90**, 094103. https://doi.org/10.1103/PhysRevB.90.094103 (2014).
34. Togo, A. & Tanaka, I. Evolution of crystal structures in metallic elements. *Phys. Rev. B* **87**, 184104. https://doi.org/10.1103/PhysRevB.87.184104 (2013).
35. Giannozzi, P. *et al.* Advanced capabilities for materials modelling with quantum ESPRESSO. *J. Phys.: Condens. Matter* **29**, 465901. https://doi.org/10.1088/1361-648x/aa8f79 (2017).
36. Perdew, J. P., Burke, K. & Ernzerhof, M. Generalized gradient approximation made simple. *Phys. Rev. Lett.* **77**, 3865–3868. https://doi.org/10.1103/PhysRevLett.77.3865 (1996).
37. Dal Corso, A. Pseudopotentials periodic table: From H to Pu. *Comput. Mater. Sci.* **95**, 337–350. https://doi.org/10.1016/j.commatsci.2014.07.043 (2014).
38. Monkhorst, H. J. & Pack, J. D. Special points for Brillouin-zone integrations. *Phys. Rev. B* **13**, 5188–5192. https://doi.org/10.1103/PhysRevB.13.5188 (1976).
39. Marzari, N., Vanderbilt, D., De Vita, A. & Payne, M. C. Thermal contraction and disordering of the Al(110) surface. *Phys. Rev. Lett.* **82**, 3296–3299. https://doi.org/10.1103/PhysRevLett.82.3296 (1999).
40. Jain, A. *et al.* Commentary: The Materials Project: A materials genome approach to accelerating materials innovation. *APL Mater.* **1**, 011002. https://doi.org/10.1063/1.4812323 (2013).
41. Zhang, Y., Kresse, G. & Wolverton, C. Nonlocal first-principles calculations in Cu-Au and other intermetallic alloys. *Phys. Rev. Lett.* **112**, 075502. https://doi.org/10.1103/PhysRevLett.112.075502 (2014).
42. Isaacs, E. B. & Wolverton, C. Performance of the strongly constrained and appropriately normed density functional for solid-state materials. *Phys. Rev. Mater.* **2**, 063801. https://doi.org/10.1103/PhysRevMaterials.2.063801 (2018).
43. Nepal, N. K., Adhikari, S., Bates, J. E. & Ruzsinszky, A. Treating different bonding situations: Revisiting Au-Cu alloys using the random phase approximation. *Phys. Rev. B* **100**, 045135. https://doi.org/10.1103/PhysRevB.100.045135 (2019).
44. Nepal, N. K., Adhikari, S., Neupane, B. & Ruzsinszky, A. Formation energy puzzle in intermetallic alloys: Random phase approximation fails to predict accurate formation energies. *Phys. Rev. B* **102**, 205121. https://doi.org/10.1103/PhysRevB.102.205121 (2020).
45. Baroni, S., de Gironcoli, S., Dal Corso, A. & Giannozzi, P. Phonons and related crystal properties from density-functional perturbation theory. *Rev. Mod. Phys.* **73**, 515–562. https://doi.org/10.1103/RevModPhys.73.515 (2001).

Acknowledgements

This study was supported by the a Grant-in-Aid for Scientific Research (C) (Grant No. 21K04628) from JSPS. The computation was carried out using the facilities of the Supercomputer Center, the Institute for Solid State Physics, the University of Tokyo.

Author contributions

S.O. did the calculations, analysed the results, and wrote the manuscript.

Competing interests

The author declare no competing interests.

Additional information

Supplementary Information The online version contains supplementary material available at https://doi.org/10.1038/s41598-021-94034-6.

Correspondence and requests for materials should be addressed to S.O.

Reprints and permissions information is available at www.nature.com/reprints.

Publisher's note Springer Nature remains neutral with regard to jurisdictional claims in published maps and institutional affiliations.